metals

MDPI

Article

Investigations on the Heat Balance of the Melt Pool during PBF-LB/M under Various Process Gases

Siegfried Baehr [1,*,†], Fabian Fritz [2,3,†], Stefan Adami [3], Thomas Ammann [4], Nikolaus A. Adams [2,3] and Michael F. Zaeh [1]

[1] Institute for Machine Tools and Industrial Management (iwb), TUM School of Engineering and Design, Technical University of Munich, Boltzmannstrasse 15, 85748 Garching, Germany
[2] Chair of Aerodynamics and Fluid Mechanics, TUM School of Engineering and Design, Technical University of Munich, Boltzmannstrasse 15, 85748 Garching, Germany; fabian.fritz@tum.de (F.F.)
[3] Energy and Process Engineering (MEP), Munich Institute of Integrated Materials, Technical University of Munich, Lichtenbergstrasse 4a, 85748 Garching, Germany
[4] Linde GmbH, Carl-von-Linde-Strasse 25, 85716 Unterschleissheim, Germany
* Correspondence: siegfried.baehr@iwb.tum.de; Tel.: +49-89-2891-5508
† These authors contributed equally to this work.

Abstract: During the powder bed fusion of metals using a laser beam (PBF-LB/M), an inert atmosphere is maintained in the build chamber to avoid reactions of the liquid metal with ambient air leading to the creation of oxides or nitrides, which alter the mechanical properties of the processed part. A continuous gas flow is guided over the process zone to remove spatters and fumes. This flow induces a convective heat transfer from the molten metal to the gas, which, depending on the level of the heat flow, may alter the melt pool dimensions by influencing the cooling rate. The present work investigated these phenomena with single-line trials, both experimentally and numerically. For this reason, a smoothed-particle hydrodynamics model was utilized to investigate the temperatures of the melt pool, cooling rates, and the integral heat balance with various gas atmospheres. In parallel, an on-axis pyrometer was set up on an experimental PBF-LB/M machine to capture the surface emissions of the melt pool. The atmosphere in the simulations and experiments was varied between argon, helium, and two mixtures thereof. The results showed a slight increase in the cooling rates with an increasing fraction of helium in the process gas. Consistently, a slight decrease in the melt pool temperatures and dimensions was found.

Keywords: additive manufacturing; laser powder bed fusion; smoothed-particle hydrodynamics; aluminum; process gases; thermal history

Citation: Baehr, S.; Fritz, F.; Adami, S.; Ammann, T.; Adams, N.A.; Zaeh, M.F. Investigations on the Heat Balance of the Melt Pool during PBF-LB/M under Various Process Gases. *Metals* **2024**, *14*, 1058. https://doi.org/10.3390/met14091058

Academic Editors: Dan Wang and Zeyu Wang

Received: 14 August 2024
Revised: 9 September 2024
Accepted: 13 September 2024
Published: 16 September 2024

1. Introduction

1.1. State of the Art

The powder bed fusion of metals using a laser beam (PBF-LB/M) is an additive manufacturing process, which enables the production of parts with high geometrical complexity and mechanical properties similar to or better than those resulting from conventional manufacturing processes. This is achieved by selectively melting the metal powder feedstock with a laser beam in a layerwise manner until the entire part is built. To avoid unwanted chemical reactions between the liquid metal and the ambient atmosphere during processing (e.g., oxidation or nitridation), the build chamber is flooded with an inert gas prior to the build job. During manufacturing, an additional laminar gas flow is directed over the process zone to remove process by-products, such as spatters and fumes. Typically, argon (Ar) or nitrogen gas is applied for this purpose. In addition to heat transfer by conduction and radiation, this gas flow leads to a convective heat transfer from the liquid metal to the gas, which, depending on the gas type and flow characteristics, alters the heat balance of the melt pool. In recent years, the influence of the gas type and gas flow on

the process capability and the part properties has been increasingly studied. Also, studies were conducted to unveil the characteristics of the heat transfer during PBF-LB/M. For this purpose, experimental as well as numerical approaches were used. Amongst the numerical approaches, the smoothed-particle hydrodynamics (SPH) method was extensively employed for simulating the PBF-LB/M process. In the following, an overview of literature relevant to this work is presented.

Various studies have investigated the influence of the gas flow and type on the PBF-LB/M process as these parameters have shown to be crucial factors for maintaining a reliable and reproducible process. A suitable gas flow velocity must be found to ensure proper removal of process by-products, such as fumes [1] and spatters [2], while not blowing away the powder bed. Ladewig et al. [2] studied the effect of a decreased gas flow velocity and found areas of increased surface roughness, which was attributed to an increased number of spatters adhering to the part surface.

These findings were extended by studies linking the gas flow velocity and uniformity to the part porosity [3]. Yang et al. [3] unveiled that a non-uniform gas flow leads to an increased porosity and lower tensile properties of the built part. The upper limits for the gas flow velocity were studied analytically by Baehr et al. [4]. The authors developed a model able to determine the powder- and gas-specific particle pickup velocity. The velocity was found to be notably higher for helium (He) compared to Ar.

Further influences of He compared to Ar on the PBF-LB/M process were unveiled. Positive effects of He and Ar–He mixtures on the cooling of spatters were found by Pauzon et al. [5]. Lower spatter temperatures were found to reduce the negative impacts of spatters on the properties of the parts, such as the surface roughness and porosity.

However, the gas flow velocity must be adapted to ensure comparable flow conditions between the gases [4]. To determine the actual gas flow velocity above the build plate and, hence, to adapt it properly, measurements, such as vane anemometer measurements as presented by Weaver et al. [6], need to be conducted.

In addition to the gas flow, various other factors influence the physical phenomena occurring in the process zone during PBF-LB/M that are highly complex and mainly controlled by heat and mass transfer. The high scanning velocity of the laser (typically around 1000 mm/s) leads to high heating and cooling rates of the melt pool (typically around 10^5–10^6 K/s), which can influence the local microstructure and, thus, properties of the part [7]. For aluminum (Al), cooling rates in the order of magnitude of 10^6 K/s were reported [8].

Within the melt pool, heat is mainly transported by convection. This is a result of the liquid metal being transported by spatial gradients of the surface tension (also known as Marangoni convection) and by buoyancy. The intensity of this flow and the level of heating influence phase-change phenomena from liquid to vapor and plasma.

Towards the environment, heat is transferred through conduction (e.g., into the underlying solidified metal), radiation into the ambient atmosphere, and convection (e.g., by the gas flow). Thermal cycles cause spatial variations to accumulate over several layers, causing inhomogeneous properties of the final part.

A common modeling approach is to neglect convection and radiation [9]. However, especially the convective heat transfer introduced by the gas flow can influence the process [9]. Masoomi et al. [9] showed that the gas flow direction relative to the laser scanning direction highly influences the convective heat transfer. An increased heat transfer was found at concurring laser scanning and gas flow directions compared to opposed directions.

In general, the SPH method is employed for the simulation of the PBF-LB/M process at the melt pool scale according to the state of the art. SPH represents the continuum by a set of particles that interact with each other through a smoothing or a filtering operation over local neighbor particles. This particle-based approach allows SPH to efficiently handle multiphase fluids. One of the essential advantages of SPH in simulating melt pool dynamics is its inherent ability to capture the material interface of an arbitrary number of neighboring phases and handle large interface deformations. Several different SPH versions have

emerged from the original SPH formulation of Gingold and Monaghan [10], such as the family of δ-SPH schemes [11], arbitrary Eulerian–Lagrange SPH [12] and Riemann-SPH [13]. Russel et al. [14] were among the first to investigate the PBF-LB/M process using SPH. Since then, SPH has emerged as a powerful tool for the simulation of PBF-LB/M and has been used in numerous studies.

Afrasiabi et al. [15] made use of the SPH method for basic investigations on the influence of varying process parameters on the melt pool dimensions during the processing of Inconel 718 via PBF-LB/M. The SPH model incorporated relevant physical phenomena, such as the recoil pressure or the Marangoni convection. In another work using SPH, Weirather et al. [16] focused on the melt pool shape and dimensions during PBF-LB/M of Inconel 718. Their SPH model was valid for the conduction-melting regime, as it neglected phenomena, such as multiple reflections, that are characteristic for the keyhole-melting regime.

1.2. Need for Action and Research Objective

Few studies have been dedicated to investigating the heat transfer phenomena during PBF-LB/M under varying atmospheres. The use of simulations is necessary to better understand the process since several melt pool features are not accessible via experiments. However, existing SPH studies and their models mainly focus on nickel-based alloys and did neither include the ambient atmosphere nor the associated heat transfer mechanisms.

The presented study aims to unveil the influence of gases with highly varying thermophysical properties (i.e., Ar, He, and two mixtures thereof) on the heat balance, dimensions, and dynamics of the melt pool in PBF-LB/M. The processing of a 2000 series Al alloy was investigated.

An existing and validated SPH simulation setup was extended by means of integrating varying atmospheres. In the first step, the experimental results were compared with the numerical results. In the second step, the simulation model was utilized to study effects that are not observable via the experiments. In particular, the differences in the heat transfer between the gases investigated and between the process with and without a gas flow were studied.

2. Numerical Modeling

2.1. Methodology

2.1.1. Fluid Dynamics Model

The fluid dynamics of the liquid melt pool and the process gas are governed by the weakly-compressible Navier–Stokes equations (e.g., Morris et al. [17]). In this work, the quasi-Lagrangian transport-velocity formulation, originally proposed by Adami et al. [18], was used. It aims to effectively cure the tensile instability, a well-known defect associated with negative pressure values regarding the ambient pressure, which ultimately leads to non-physical particle clustering, numerical fragmentation, and severe instability problems [19]. This is achieved by introducing an additional velocity by which the particles are being advected.

The continuous surface force model [20] was utilized to represent surface tension effects between multiple phases with distinct interfaces. This work used the density-partitioned stress-based formulation of Zöller et al. [21], which implicitly incorporates Marangoni stresses and allows for a larger time step size in comparison to prior stress-based formulations due to density weighting of the surface stress. Additionally, it shows excellent agreement for flows dominated by capillary and Marangoni forces for high density ratios and high physical viscosities.

2.1.2. Heat Transfer Model

The evolution of the temperature in the solid substrate, in the liquid melt pool, and in the process gas was described by the conservation of energy. In a Lagrangian formalism,

where the material or Lagrangian derivative with the momentum velocity $\mathbf{u}$ is $\frac{\mathrm{d}}{\mathrm{d}t} = \frac{\partial}{\partial t} + \mathbf{u}\cdot\nabla$, the transport of enthalpy is given with the density ρ by [16]

$$\rho \frac{\mathrm{d}h}{\mathrm{d}t} = -\mathrm{div}\mathbf{q} + \dot{\omega}_\mathrm{v} + \dot{\omega}_\mathrm{l} + \dot{\omega}_\mathrm{r}. \tag{1}$$

The enthalpy h and the temperature T are coupled through

$$h(T) = \int_{T^0}^{T} C_\mathrm{p}(\vartheta)\,\mathrm{d}\vartheta, \tag{2}$$

where T^0 denotes an arbitrary reference temperature and C_p denotes the temperature-dependent specific heat capacity. The conductive heat flux is $\mathbf{q} = -k\nabla T$ and the volumetric heat sources for evaporative cooling, energy transfer by the laser, and heat radiation are $\dot{\omega}_\mathrm{v}$, $\dot{\omega}_\mathrm{l}$, and $\dot{\omega}_\mathrm{r}$, respectively. The temperature-dependent thermal conductivity is denoted by k.

The SPH discretization of the divergence of the conductive heat flux in the transport Equation (1) follows the work of Cleary et al. [22,23], which ensures continuity of the heat flux across discontinuous material properties.

The maximum surface temperature of the melt pool can easily reach its boiling temperature as a consequence of the laser-induced heating, leading to an increased evaporation rate of the liquefied metal. The work described here utilized the simplified evaporation model of Anisimov and Khokhlov [24], which has been successfully applied before (e.g., Khairallah et al. [25], Semak et al. [26,27], and Weirather et al. [16]). The model does not explicitly resolve the transition from liquid to vapor but models the vapor recoil pressure onto the liquefied metal [28]. Considering melt removal due to evaporation negligible in favor of the hydrodynamic mechanism induced by the recoil pressure is a reasonable assumption as long as the evaporation rate is low enough to produce a noticeable recoil pressure [27], which, as noted by Khairallah et al. [25], is typically the case in PBF-LB/M. For a detailed description of the utilized evaporation model within the SPH framework, the reader is kindly referred to the work of Weirather et al. [16].

The primary driving mechanism of the PBF-LB/M process is the energy input into the material due to laser illumination on its surface. Consequently, a sufficient description of the laser beam is of prime interest for accurately modeling the melt pool dynamics. Several models with increased computational demand and complexity exist for describing the laser–material interaction. The ray tracing method was used in this work to accurately describe both absorption and reflection, while being computationally feasible at the same time. At its core, ray tracing consists of approximating the laser with discrete rays and tracking those rays geometrically along their path in space, which only change due to reflection or refraction on an interface. The ray tracing method has been utilized in traditional Eulerian schemes with great success as it provides a more generic laser beam model than a simple heat source [16] but is more affordable than solving Maxwell equations [29] (e.g., in the works of Khairallah et al. [30,31] and Zenz et al. [32]). In this work, a methodology similar to that of Shah et al. [33,34] was used, who developed a combined SPH and ray tracing method to study the keyhole formation in laser drilling [33,34] and PBF-LB/M [34] of stainless steel and aluminum, respectively. The proposed methodology does not require an explicit interface representation; therefore, it puts no constraints on the topological evolution of the material interface, making their method a more natural fit to SPH than previous attempts.

The radiative cooling is typically described by the Stefan–Boltzmann relation for black-body radiation. However, since the heat losses due to radiation are typically small in PBF-LB/M [35], the source term was not included in this work.

2.1.3. Integral Heat Balance

An integral formulation of the enthalpy transport Equation (1) reads

$$\underbrace{\int_{\mathcal{M}(t)} \frac{\mathrm{d}h}{\mathrm{d}t}\,\mathrm{d}m}_{\equiv \dot{H}} = \underbrace{-\oint_{A(t)} \mathbf{q}\cdot\mathbf{n}\mathrm{d}A}_{\equiv \dot{Q}} + \underbrace{\int_{V(t)} \dot{\omega}_\mathrm{v}\,\mathrm{d}V}_{\equiv \dot{\Omega}^v} + \underbrace{\int_{V(t)} \dot{\omega}_\mathrm{l}\,\mathrm{d}V}_{\equiv \dot{\Omega}^l}, \tag{3}$$

where V denotes the control volume (CV), and A and $\mathcal{M}$ its surface area and mass, respectively. The heat flow rate is abbreviated as $\dot{Q}$, and the volume integrals of the heat sources are abbreviated as $\dot{\Omega}$. The heat flow rate incorporates the heat flux through conduction explicitly and the heat flux through convection implicitly, as convection leads to an increased heat transfer across the surface of the CV due to the Lagrangian transport of enthalpy in the fluid phase. Positive heat flow rates ($\dot{Q} > 0$) correspond to heat being transferred into the CV, and negative heat flow rates ($\dot{Q} < 0$) correspond to heat being withdrawn from the CV. Positive integral heat sources ($\dot{\Omega} > 0$) correspond to net heating, and negative integral heat sources ($\dot{\Omega} < 0$) to net cooling of the CV. For steady-state simulations, the heat flow rate and integral heat sources are balanced, and the total enthalpy transfer rate $\dot{H}$ approaches zero (i.e., $\dot{H} \to 0$).

The integral heat balance Equation (3) was applied to the melt pool in this work. Thus, the integral heat balance equation reads

$$\dot{H}_\mathrm{M} = \dot{Q}_{\mathrm{M}\to\mathrm{S}} + \dot{Q}_{\mathrm{M}\to\mathrm{G}} + \dot{\Omega}^v_\mathrm{M} + \dot{\Omega}^l_\mathrm{M}. \tag{4}$$

The heat flow rate $\dot{Q}_\mathrm{M}$ over the melt pool surface A_M was split up into the heat flow rates through the melt–substrate interface $\dot{Q}_{\mathrm{M}\to\mathrm{S}}$ and through the melt–gas interface $\dot{Q}_{\mathrm{M}\to\mathrm{G}}$, respectively. The utilized SPH discretization of the heat flow rate is given in Appendix A.1.

2.2. Numerical Setup

The PBF-LB/M process parameters and conditions used for the numerical simulations presented in this work are summarized in Table 1. The given values are in accordance with the experimental setup.

The computational domain used in this work is shown in Figure 1.

The simulations were performed on an initial Cartesian lattice particle distribution, where the initial particle spacing was $\Delta x = 6\,\mu\mathrm{m}$. The smoothing length h was equal to the characteristic particle spacing (i.e., $h = \Delta x$). The chosen resolution ensured that the melt pool was at least discretized by 30 particles along its width when steady-state was reached. The final time of the simulation was set to $t_\mathrm{f} = 1.25\,\mathrm{ms}$, which allowed the laser to travel 1000 µm within the simulation time. This ensured that the melt pool reached steady-state behavior. The artificial speed of sound was set to $c_0 = 50\,\mathrm{m\,s^{-1}}$, which limited density fluctuations to the incompressible regime, where the weakly-compressible equation of state used in this work is valid.

Table 1. The process parameters used throughout this work for the numerical simulation.

Process Parameter	Value	Units
Scan speed, v	0.8	$\mathrm{m\,s^{-1}}$
Laser power, P	200	W
Laser spot size radius, r_σ	40	µm
Laser wavelength, λ	1064	nm
Gas flow velocity, u_∞	1.5	$\mathrm{m\,s^{-1}}$
Atmospheric pressure, p_∞	1×10^5	Pa
Ambient temperature, T_∞	600	K
Gravitational acceleration, g	9.81	$\mathrm{m\,s^{-2}}$

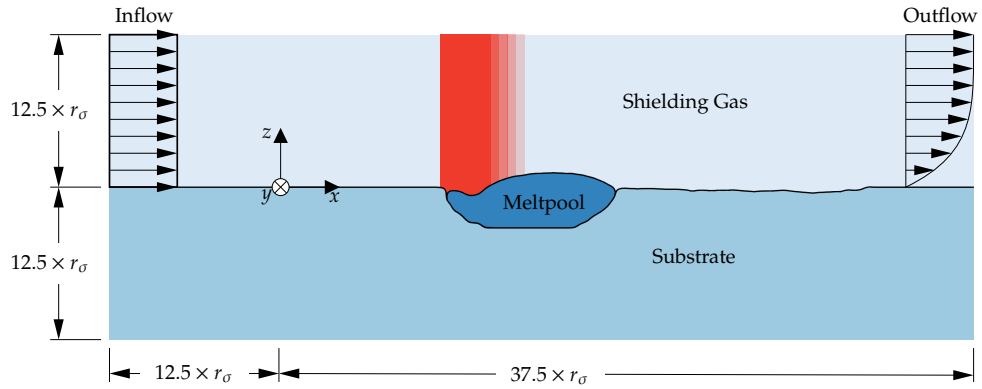

Figure 1. Cross-sectional view of the computational domain for the PBF-LB/M SPH process simulation. The red area indicates the laser beam. The extend of the domain into the y-direction was $25 \times r_\sigma$; negative x: scanning direction.

Both the temperatures of the process gas and the substrate were initially set to $T_\infty = 600\,\mathrm{K}$, which accounted for the heating due to previously built layers during the process. This was shown by Jadhav et al. [36], who measured the system temperature experimentally for a pure copper process.

The wall boundary conditions were enforced by the utilization of the methodology proposed by Adami et al. [37], which constraints particles in the vicinity of the walls to a fixed temperature $T_\mathrm{walls} = T_0$ and a slip boundary condition for the velocity. The fluid phases were enclosed in all directions by wall boundary conditions apart from the inflow and outflow boundaries. The in- and outflow boundary conditions used the methodology of Lastiwka et al. [38], where particles are being injected with an inflow velocity $u_\mathrm{inflow} = 1.5\,\mathrm{m\,s^{-1}}$ and inflow temperature $T_\mathrm{inflow} = T_0$ at the inlet and are being removed from the computational domain at the outlet without generating excessive waves. The wall as well as the in- and outflow region were discretized using at least three particle layers, which ensured full support for the fluid particles in the vicinity of those regions and for the chosen quintic spline kernel [39]. An isothermal slip-wall boundary condition was used on the top of the computational domain.

The powder layer was not taken into consideration in this work to reduce the computational effort of the parameter study. It was shown in preliminary studies and in the literature that this does not affect the results significantly [40]. Thereby, less spatial resolution was needed in comparison to simulations that fully resolve the powder particles.

2.3. Macroscopic Material Properties

The macroscopic material properties for the used Al alloy are given in Table A1 in the Appendix B. A linear fit was used for the temperature-dependent surface tension coefficient. The dynamic viscosity (The nominal viscosity of the liquid Al alloy was twenty times as high in the simulation compared to the presented value given in Table A1 in the Appendix B for improved numerical stability of multiphase flows with high density ratios and low absolute viscosities (see, e.g., Russel et al. [14] or Weirather et al. [16]).) was evaluated using an Arrhenius fit. The surface tension coefficients between the liquid Al alloy and Ar and between the liquid Al alloy and He were considered identical.

The temperature-dependent absorptivity of the laser was obtained from the electrical resistivity of the material and the wavelength of the laser by using the Hagen–Ruben relationship [41].

The temperature-dependent values for the material are given in Table A2 in the Appendix B. A linear interpolation was used for temperature values between the tabulated data. A constant extrapolation for the thermal conductivity and specific heat capacity was used for temperature values outside the given range, and a linear extrapolation was used for the enthalpy.

The macroscopic material properties for the process gases Ar and He are given in Table A3 in the Appendix B. A polynomial fit for the thermal conductivity and a power function for the dynamic viscosity were used (see Figure 2). The density and the specific heat capacity were assumed to be constant over the temperature range. A volume-weighted average was used for the Ar-He gas mixtures. For example, the thermal conductivity for such a gas mixture was calculated by

$$k(T) = \sum_{\alpha} k_{\alpha}(T) X_{\alpha}, \tag{5}$$

where X_{α} denotes the volume fraction of the pure gas components. The density, the dynamic viscosity, and the specific heat capacity were calculated analogously.

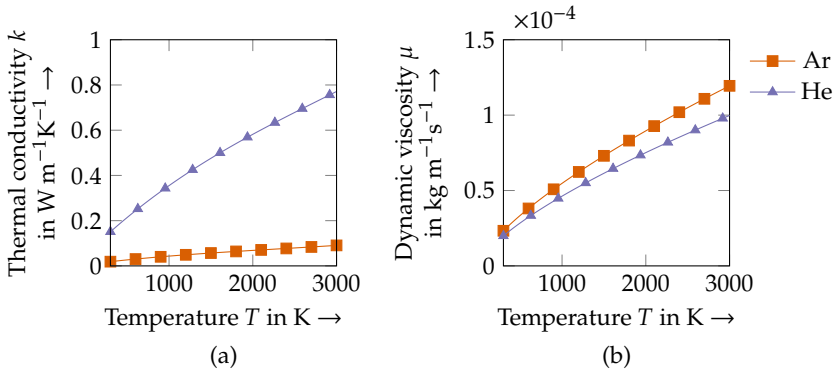

Figure 2. Temperature-dependent material properties for different process gases. (**a**) a polynomial fit for the thermal conductivity k and (**b**) a power function for the dynamic viscosity μ for argon (Ar) and helium (He) from 300 K to 3000 K.

3. Experiments

3.1. Experimental Setup

All experiments in this study were conducted in a lab-scale PBF-LB/M machine (AconityMINI, Aconity3D GmbH, Aachen, Germany). The machine was equipped with a 500 W fiber laser with a wavelength λ of 1064 nm and a laser spot diameter of 80 µm with a Gaussian energy distribution. The build plate measured a diameter of 140 mm. A picture of the experimental setup used is given in Figure A1 in the Appendix C. A Zr-blended 2000 series Al alloy with a particle size distribution of 20–60 µm was used as the powder material. Its chemical composition, provided by the manufacturer, is given in Table 2.

Table 2. Chemical composition of the Zr-blended 2195 aluminum alloy [42].

Element	Aluminum (Al)	Copper (Cu)	Lithium (Li)	Magnesium (Mg)	Silver (Ag)	Zirconium (Zr)
wt%	Bal.	4.0	1.0	0.5	0.4	1.8

The build job layout for the experiments consisted of three randomly distributed cubes with a size of 10 mm × 10 mm × 8 mm with two single lines each on the top layer (see Figure 3). The laser power P and the scan speed v as given in Table 1 were applied. This parameter combination has reportedly shown to provide a stable process window for Al single lines [43]. The hatch distance h and the layer thickness t were set to 80 µm and 30 µm, respectively. This resulted in a volumetric energy density $VED = \frac{P}{vht}$ of approximately 104 J/mm³. The scanning strategy was parallel stripes with a rotation of 67° per layer. This parameter combination showed a high relative density of >99.5% in preliminary trials. For the build jobs, four gases were applied with a velocity u_{∞} of 1.5 m/s: Ar, He, 70 vol.-% Ar + 30 vol.-% He (ArHe30), and 30 vol.-% Ar + 70 vol.-% He (ArHe70). The oxygen level within the build chamber was kept below 500 ppm.

After the build job, the cubes were sawed off the build plate and were further processed via metallography. Firstly, they were cold embedded using a resin (EpoFix Resin, Struers GmbH, Willich, Germany) and a hardener (EpoFix Hardener, Struers GmbH, Willich, Germany) in a ratio of 25:9. The subsequent grinding and polishing followed a four-step procedure: (1) grinding with a 220 grit grinding paper, (2) 9 µm polishing, (3) 3 µm polishing, (4) 1 µm polishing. In the final post-processing step, the cubes were chemically etched for 15 s by the immersion technique using an etchant consisting of HNO_3, HCl, and HF in water (Keller-Wilcox, Bernd Kraft GmbH, Wetzlar, Germany). To measure the penetration depth of the single lines, the etched cubes were measured by optical light microscopy (VHX-5000, Keyence Deutschland GmbH, Neu-Isenburg, Germany). The measuring procedure and a top view indicating the fabricated single lines are depicted in Figure 4.

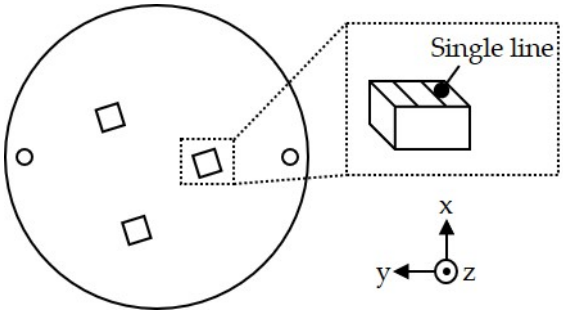

Figure 3. Schematic top view of the build plate showing the build job layout (not to scale); x: recoating direction, y: gas flow direction, z: building direction.

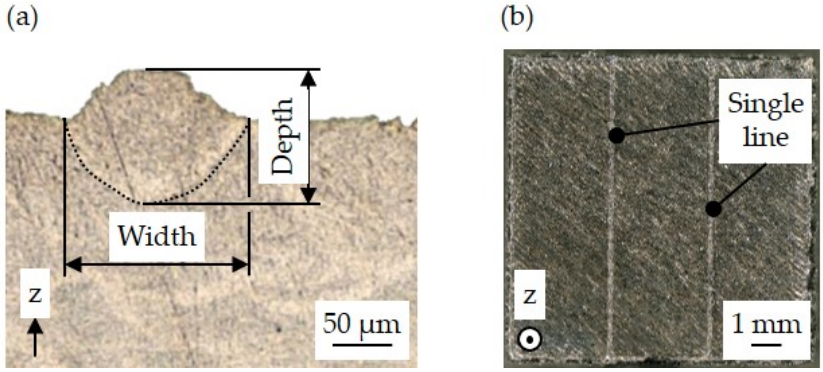

Figure 4. (**a**) Cross-sectional view of an etched single line melt pool outlining the measurement of the melt pool width and depth (the melt pool is indicated by a black dotted line), (**b**) top view of a fabricated cube showing the single lines; z: building direction.

3.2. Pyrometry Setup and Data Analysis

The machine was equipped with an on-axis high-speed pyrometer (KG 740-LO, KLEIBER Infrared GmbH, Unterwellenborn, Germany). The spectral range of the device lay in a range between 1450 and 1700 nm and its response time t_{95} was 6 µs at a frequency of 100 kHz. Considering the size of the specimens and the scanning speed, approximately 150,000 data points were sampled per layer (depending on the stripe angle). A dichroic mirror in the scanner unit ensured the trespassing of the respective heat radiation from the process zone.

Due to a lack of knowledge about the temperature-dependent emission coefficient of the Al alloy, no calibration of the pyrometer signal was performed for real temperatures. Only relative changes that correlated with variations in the surface temperature were considered in the investigations. Thus, as suggested by [44], the pyrometry results shown in this study are given in non-dimensional values of digital numbers (DN) ranging from 0 to 900 DN. At no laser illumination, the signal oscillated by as much as 1 DN, which is

why this was assumed to be the noise level of the pyrometry measurements. Any values below 1 DN were excluded from the analysis.

The measuring spot had a diameter of about 200 µm in the setup used. A simplified scheme of the experimental setup is given in Figure 5. It shows the optical path of the setup and a magnified process zone outlines possible sources of heat radiation detected by the pyrometer: the melt pool, the by-products (fumes and spatters), and the surface of the current layer.

The pyrometer signals were stored in a point cloud data (PCD) file. The software MATLAB was applied to evaluate the PCD files (R2021a, Mathworks Inc., Natick, MA, USA). The mean values of the data were considered to compare the influences of the various gases on the heat balance of the melt pool.

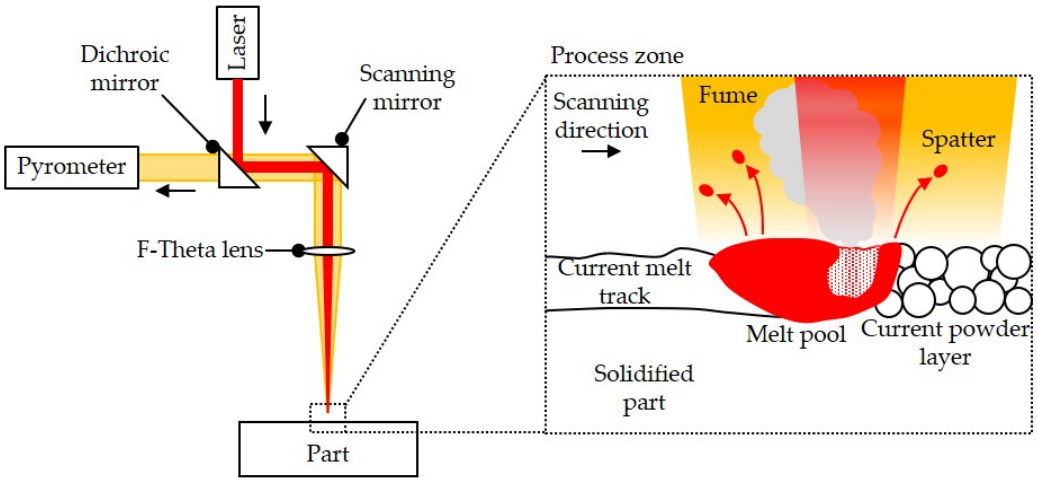

Figure 5. Schematic representation of the pyrometry setup.

4. Results and Discussion

In the following, the experimental and the numerical results are presented and discussed to study the efficacy of various process gases to alter the heat transfer during PBF-LB/M. The numerical methodology outlined in Section 2 was first compared to the measurements from the experimental setup outlined in Section 3. Subsequently, the numerical results were exploited to study features that are impossible to study experimentally due to the limited spatial and temporal resolution of real-world experiments. If not stated otherwise, the numerical analysis was performed at the final simulation time where the melt pool has reached steady-state status.

4.1. Comparison of Experimental and Numerical Results

4.1.1. Surface Temperature of the Melt Pool

Figure 6 depicts the results from the pyrometer measurements. For the representation, the moving average with a period of ten of the mean values of the pyrometer data calculated per layer was displayed. The results showed that the heat radiation emitted from the processing zone differed only slightly between the gases studied. With an increasing fraction of He in Ar, decreasing temperatures were found. Also, an increasing temperature between the start of the build job at 0 mm and a build height of 1 mm could be observed. After that, a stationary temperature established itself. This is typical for the PBF-LB/M process and was described, for example, by Chaudry et al. [45]. In the first layers, an intense heat conduction into the build plate occurs. With an increasing build height, this effect decreases, and additionally, the isolating powder bed prevents further cooling by convection. Thus, heat accumulation appears.

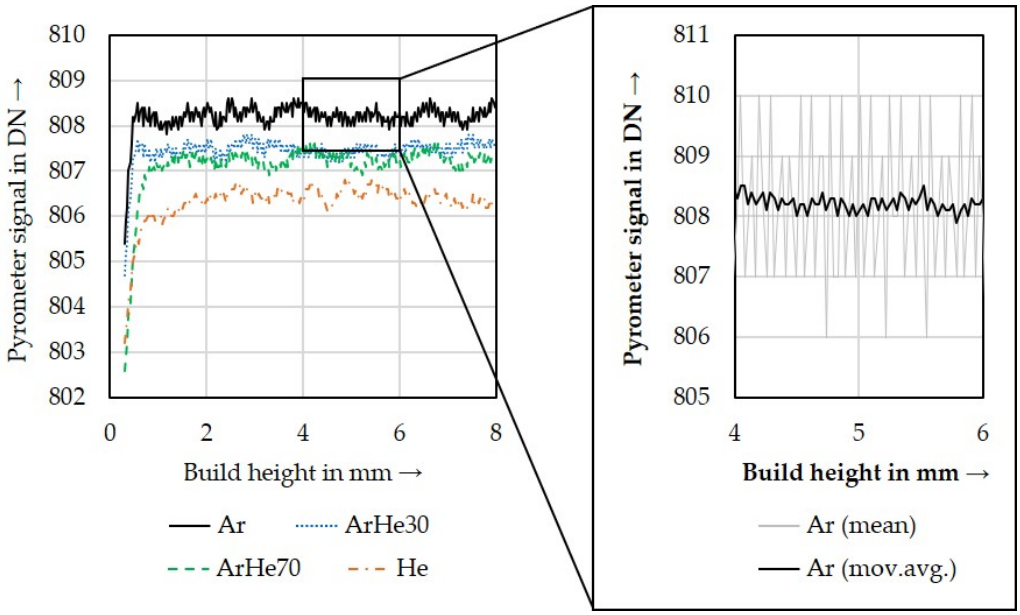

Figure 6. Moving average (mov.avg.) of the mean values of the pyrometer signal depending on the process gas; Ar: argon, He: helium, ArHe30/70: 70/30 vol.-% Ar + 30/70 vol.-% He.

The mean values and the standard deviations of the average surface temperatures of the melt pools from simulations with and without gas flow are given in Table 3. The data were evaluated over the time interval $t_{\text{sample}} = [1.15\,\text{ms}, 1.25\,\text{ms}]$ using $\Delta t_{\text{sample}} = 1 \times 10^{-6}\,\text{s}$. The evaluation approach of the average surface temperature in SPH is given in the Appendix A.2. As it can be seen in Table 3, the temperature slightly decreased monotonically from Ar to He for simulations with $u_\infty = 0.0\,\text{m}\,\text{s}^{-1}$, which was in accordance with the pyrometer measurements given in Figure 6. The presence of a gas flow with $u_\infty = 1.5\,\text{m}\,\text{s}^{-1}$ reduced the average surface temperature. However, the gas flow introduced additional noise to the measurements of the average surface temperature. Thus, there was no clear trend observed between the different compositions of the gas flow in this case.

Table 3. Mean values and standard deviations of the surface-average temperatures of the melt pool received from the simulation depending on the process gas; Ar: argon, He: helium, ArHe30/70: 70/30 vol.-% Ar + 30/70 vol.-% He.

Condition	Ar	ArHe30	ArHe70	He	Unit
$u_\infty = 0.0\,\text{m}\,\text{s}^{-1}$	1206.8 ± 0.4	1204.9 ± 0.5	1204.0 ± 0.3	1203.8 ± 0.3	K
$u_\infty = 1.5\,\text{m}\,\text{s}^{-1}$	1195.0 ± 3.3	1195.8 ± 2.5	1194.8 ± 3.7	1195.0 ± 2.6	K

4.1.2. Melt Pool Dimensions

The results from the measurements of the melt pool dimensions in the case of a gas flow are summarized in Figure 7. The mean data received from the experiments and simulations of each gas are depicted with their standard deviations. As it can be seen, the widths of the melt pools were generally larger compared to the depths for all gases. This indicated a conduction melting regime during the process in accordance with the study of Kempen et al. [46]. Only little differences occurred between the gases for the melt pool widths and depths. The experimentally determined melt pool widths and depths varied in the range of 180–195 µm and 141–160 µm, respectively. Also, decreasing values of the standard deviation of the melt pool depth measurements could be observed from Ar to He in the experiments. The numerical results showed widths in the range of 214–217 µm and depths in the range of 103–106 µm. In addition to the experimental data, the melt pool lengths could be extracted from the simulations. These are depicted in Figure 7 but showed no significant differences between the gases.

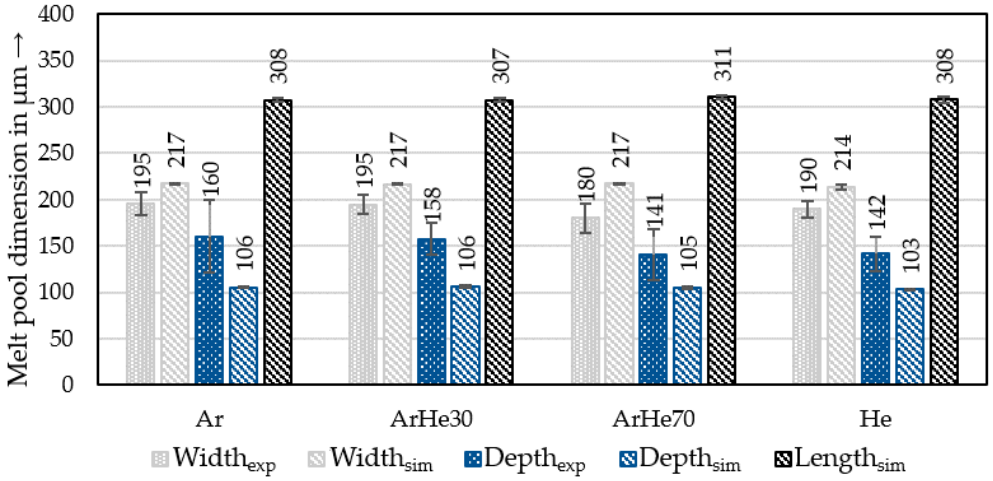

Figure 7. Mean values of the melt pool dimensions depending on the process gas; Ar: argon, He: helium, ArHe30/70: 70/30 vol.-% Ar + 30/70 vol.-% He.

The melt pool dimensions showed only a weak dependence on gas properties for the numerical simulation as well as the experiments, which was in accordance with the surface temperature measurements. The marginally lower values of the melt pool width and depth under He compared to Ar could be correlated to the marginally higher heat transfer under He compared to Ar.

4.2. Numerical Investigation of the PBF-LB/M Process Zone

In the following, the simulation results obtained from the validated methodology outlined in Section 2 are evaluated. The Ar-He gas mixtures were omitted from the presented figures for the sake of clarity.

4.2.1. Melt Pool Temperature and Flow Field

The temperature fields and melt pool morphologies through the *x*-*z* plane for Ar and He are shown in Figure 8 for different gas flow conditions (i.e., with and without gas flow). No significant differences in the melt pool shapes were observed for all investigated process gases and flow conditions. Therefore, it can be concluded that the increased heat transfer between the gas and the melt pool due to convection has no significant influence on the dynamics of the melt pool.

The temperature distributions in the melt pool and in the substrate only differed marginally for all investigated atmosphere conditions. In contrast, the temperature distributions in the gas were found to be significantly different due to the different material properties and transport coefficients of Ar and He. The temperature field in the gas phase for simulations with gas flow was being advected in the direction of the flow in comparison to the case without gas flow.

Close to the interaction zone between the laser beam and the melt pool, the highest temperatures of up to approximately 2800 K were found. The temperature gradient towards the substrate in the negative *z*-direction was higher compared to the temperature gradient towards the gas phase (i.e., the ambient temperature of 600 K was reached closer to the melt pool in the substrate than in the gas phase). This indicated higher cooling rates due to a comparably higher heat transfer by conduction in the solid material, which is discussed in more detail in Section 4.2.2.

The fluid flow within the melt pool is dominated by the Marangoni convection, as described in Section 1. It drives the flow from the hot laser-induced heating zone towards colder regions on its surface and produces a reversed flow within the melt. No significant effects of the investigated process gases and flow conditions on the melt pool flow were found under the assumption of equal surface tension coefficients between the liquid Al and Ar and between the liquid Al and He.

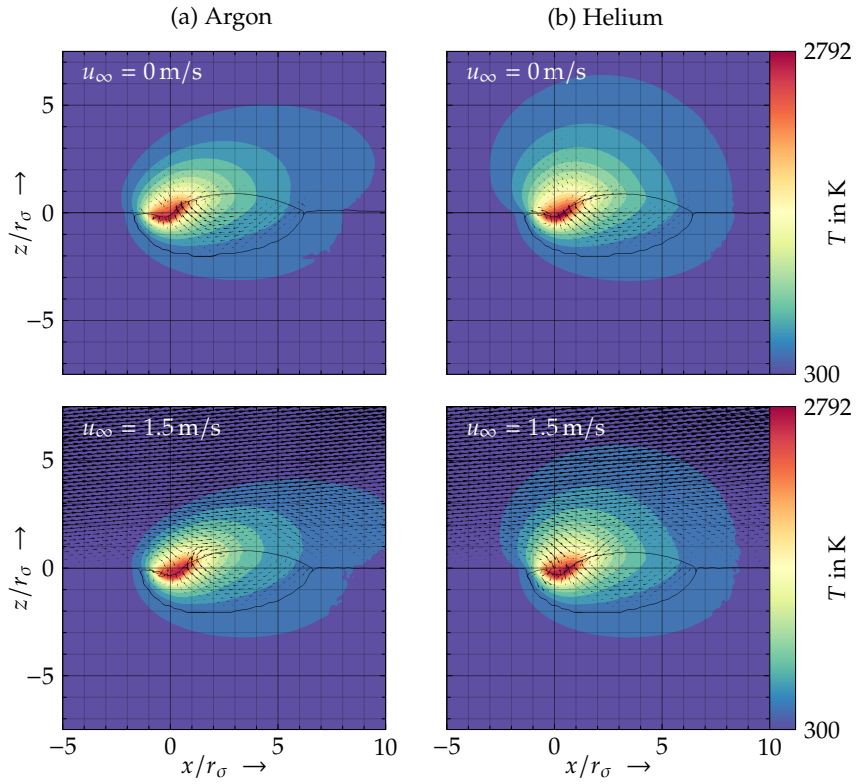

Figure 8. Cross-sectional view of the melt pool (x-z plane) under various gas flow settings (with and without gas flow) depicting the temperature fields and flow velocity arrows; (**a**) argon, (**b**) helium.

4.2.2. Heating and Cooling Rates

The absolute temperature rate-of-change fields (i.e., the heating and cooling rates) in a logarithmic scale through the x-z plane for Ar and He and different flow conditions (i.e., with and without gas flow) are given in Figure 9. The thermal gradients and cooling rates are essential metrics for assessing the manufacturing process as they are responsible for the final microstructure that is characteristic for PBF-LB/M [47]. The spatial distribution of heating and cooling rates is generally unavailable from an experiment and can only be investigated from a numerical simulation.

In this work, the heating and cooling rates were used to investigate the influence of the surrounding process gas on the liquid melt and solid substrate.

For all gases studied, globally similar heating and cooling rates were found. The highest heating rates of up to 10^8 K/s appeared close to the interaction zone of the laser beam and the melt pool. With an increasing distance from this area in the negative x-direction, the heating rates decreased until they reached values in the order of magnitude of 10^6 K/s. Passing the black iso-surface in the positive x-direction, which separates zones of heating and cooling, the liquid metal started to cool due to heat conduction and convection. Similar cooling rates in the range of 10^6–10^7 K/s were found in all cases. The observation of higher temperature gradients towards the substrate compared to the ones towards the gas phase in Figure 8 could be related to similar higher gradients in the temperature rates found in Figure 9.

Considering the cooling rates in the vicinity of the melt pool surface, comparable values as those received in an experimental study in the order of magnitude of 10^6 K/s were determined [47]. Hooper et al. [47] applied a high-speed thermography method to determine the cooling rates during the processing Ti6Al4V. Also, the melt pool surface cooling rates determined numerically by Li et al. [8] for Al processed via PBF-LB/M of 10^6 K/s could be related to the results given in Figure 9.

The temperature rates in the substrate only differed marginally between the different process gases and gas flow conditions. The temperature rates in the gas and in the melt

pool were, however, heavily influenced by the choice of the atmosphere conditions. The iso-surface bent more in the direction of the flow for simulations with forced gas flow than for simulations without. Consequently, the temperature rate distributions were different in the vicinity of the melt–gas interface.

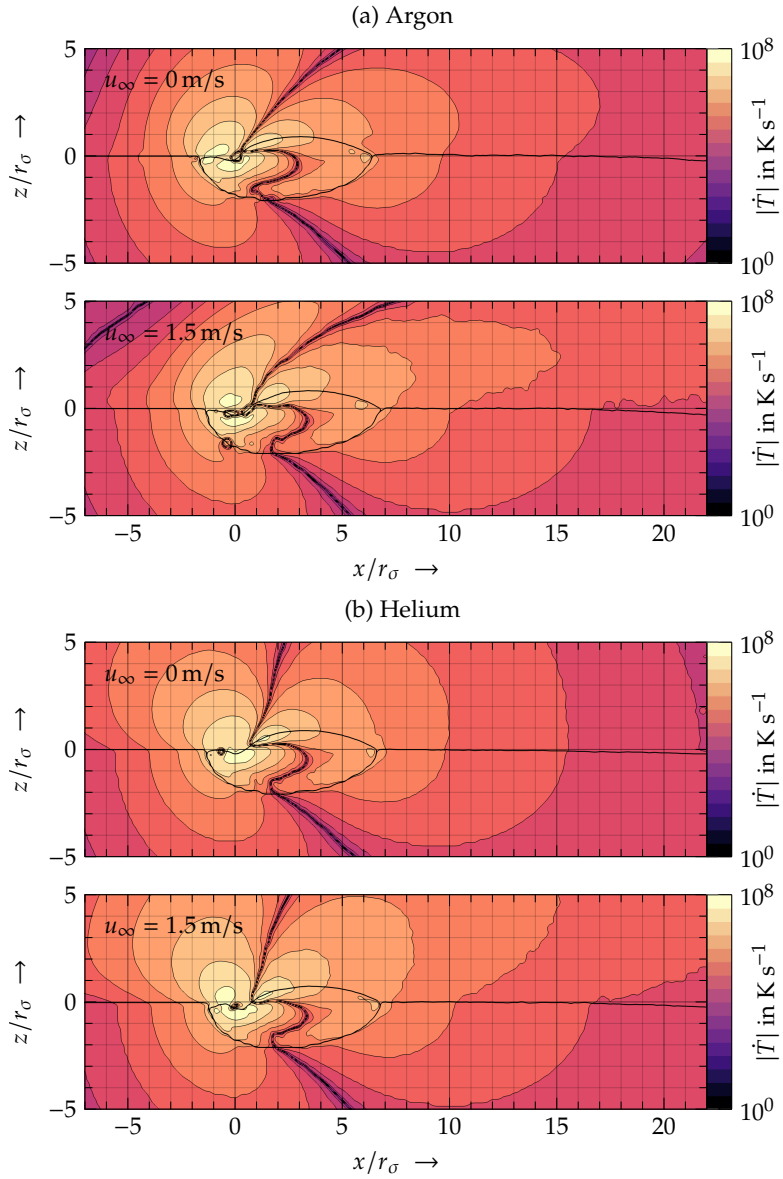

Figure 9. Cross-sectional view of the melt pool (x-z plane) under various gas flow settings (with and without gas flow) with the absolute temperature rate-of-change fields $|\dot{T}|$ in a logarithmic scale; the zones of heating ($\dot{T} > 0$) and cooling ($\dot{T} < 0$) are separated by the converging iso-contour lines for decreasing values of $|\dot{T}|$, where $|\dot{T}|$ approaches zero rapidly; (**a**) argon, (**b**) helium.

The differences in the temperature rates in the mushy zone, which is the zone around the melt pool where the material has neither been fully melted nor solidified, are expected to be reflected in the mechanical properties of the final part as they affect the local microstructure formation. Such temperature effects have already been reported in [48] for other materials.

4.2.3. Evaluation of the Integral Heat Balance

The individual contributions to the heat balance of the melt pool, as evaluated following the methodology outlined in Section 2.1.3, are given in Table 4 for Ar, ArHe30, ArHe70,

and He at steady-state with gas flow. The data were evaluated and averaged over the time interval $t_{\text{sample}} = [1.15\,\text{ms}, 1.25\,\text{ms}]$ using $\Delta t_{\text{sample}} = 1 \times 10^{-6}\,\text{s}$.

Table 4. Evaluation of the integral heat balance (mean values with standard deviations) for the PBF-LB/M process with gas flow; Ar: argon, He: helium, ArHe30/70: 70/30 vol.-% Ar + 30/70 vol.-% He, $\dot{H}_{\text{M}}$: total enthalpy transfer rate, $\dot{Q}_{\text{M}\to\text{G}}/\dot{Q}_{\text{M}\to\text{S}}$: heat flow rates between melt and gas/substrate, $\dot{\Omega}^{v}_{\text{M}}$: cooling through the evaporation of liquid metal, $\dot{\Omega}^{l}_{\text{M}}$: energy transferred into the melt pool through laser illumination.

Parameter	Ar	ArHe30	ArHe70	He	Unit
$\dot{H}_{\text{M}}$	-0.766 ± 0.690	-0.888 ± 0.771	-0.833 ± 1.269	-0.619 ± 0.648	W
$\dot{Q}_{\text{M}\to\text{G}}$	-1.902 ± 0.147	-2.062 ± 0.381	-2.077 ± 0.305	-2.146 ± 0.203	W
$\dot{Q}_{\text{M}\to\text{S}}$	-40.74 ± 0.263	-40.25 ± 0.369	-41.06 ± 0.384	-40.28 ± 0.416	W
$\dot{\Omega}^{v}_{\text{M}}$	-0.194 ± 0.116	-0.179 ± 0.098	-0.199 ± 0.126	-0.177 ± 0.086	W
$\dot{\Omega}^{l}_{\text{M}}$	$+42.07 \pm 0.564$	$+41.61 \pm 0.402$	$+42.51 \pm 0.989$	$+41.98 \pm 0.387$	W

It was found that the total enthalpy transfer rate of the melt pool was relatively small in comparison to the energy transfer into the material by laser illumination for all investigated process gases (i.e., $|\dot{H}_{\text{M}}| \ll |\dot{\Omega}^{l}_{\text{M}}|$). Thus, the heat flow rates and integral heat sources were balanced and the steady-state assumption was justified.

The average heat flow rate of the melt through the melt–gas interface $\dot{Q}_{\text{M}\to\text{G}}$ showed an increased heat flow for process gases with an increased He content. That means that the heat flow rate with Ar was the smallest in comparison to the heat flow rate of He, which was the highest. However, even though a trend towards increased heat flow rates with an increased He content was observable, the differences were still small. The average heat flow rate of the melt through the melt–substrate interface $\dot{Q}_{\text{M}\to\text{S}}$ was comparable for all investigated process gases. No clear trend for an increasing He or Ar content was observable.

The heat flow rates through the melt–gas and the melt–substrate interfaces contributed with approximately 5% and 95%, respectively, to the total heat flow rate. Therefore, the absolute heat flow rate through the melt–gas interface was much smaller than the one through the melt–substrate interface (i.e., $|\dot{Q}_{\text{M}\to\text{G}}| \ll |\dot{Q}_{\text{M}\to\text{S}}|$).

The cooling through the evaporation of liquid metal was small ($\dot{\Omega}^{v}_{\text{M}} < 1\,\text{W}$) in comparison with the competing heat transfer mechanisms in the melt pool and showed no significant differences between the investigated process gases.

The energy transferred into the melt pool through laser illumination was $\dot{\Omega}^{l}_{\text{M}} \approx 42\,\text{W}$ for all investigated process gases. Considering the nominal laser output power of 200 W, this resulted in an effective absorptivity of $\alpha_{\text{eff}} \approx 0.238$ despite the relatively low nominal absorptivity of Al ($\alpha \approx 0.0588$ at room temperature [41]) due to the elevated absorptivity at high temperatures.

The energy transferred into the solid substrate through laser illumination was $\dot{\Omega}^{l}_{\text{S}} \lesssim 0.1\,\text{W}$. This means that the laser almost exclusively illuminated the liquid melt in the steady-state process window.

5. Conclusions

The goal of this study was to investigate the heat transfer mechanisms during the powder bed fusion of metals using a laser beam (PBF-LB/M) under various atmospheres. The four gases argon (Ar), helium (He), 70 vol.-% Ar + 30 vol.-% He, and 30 vol.-% Ar + 70 vol.-% He were investigated. A validated smoothed-particle hydrodynamics (SPH) model was utilized to simulate the processing of a high-strength aluminum alloy via PBF-LB/M. The high-fidelity model considers all relevant physical phenomena occurring in the PBF-LB/M process zone, such as evaporation, surface tension, and Marangoni convection. The laser beam is modeled using a detailed ray-tracing methodology to take multiple reflections of the laser beam with the melt pool surface into account.

In the first step, the SPH model results were compared to experimental results to evaluate its capability to represent the given use case. This was conducted by comparing the melt pool dimensions and the melt pool surface temperatures obtained by metallography and pyrometry, respectively, with the associated values extracted from the numerical model. Then, the simulation model was utilized to study heat transfer phenomena that are not available via experiments. The melt pool flow and temperatures as well as the heating and cooling rates within the melt pool were investigated in particular. Finally, an integral heat balance was applied to quantify the heat transfer between melt and gas and between melt and substrate. The main conclusions of the study can be summarized as follows:

- The employed SPH model is suitable for representing the experimental PBF-LB/M process. In both approaches, simulation and experiment, only a small dependency of the process to varying gas compositions was found. A slight trend towards lower surface temperatures and lower melt pool dimensions with an increasing fraction of He in the process gas was observed.
- The temperature fields in the melt pools and substrates, as well as the melt pool flows received from the SPH simulation, showed only small differences for the four gases. With an increasing fraction of Ar in the process gas, the temperature field was advected more strongly in the direction of the gas flow.
- The temperature rate-of-change distribution close to the melt-gas surface was strongly influenced by the gas flow setting (i.e., with or without gas flow) but only showed small differences between the four gases.
- With an increasing fraction of He in the process gas, the heat flow rate through the melt–gas interface increased. The heat flow rate through the melt–substrate interface was comparable for all gases studied.

The results highlighted that the heat transfer in the PBF-LB/M process zone is mainly influenced by heat conduction (i.e., the heat flow rate between the substrate and melt pool), whereby using a gas flow has additionally shown to change the temperature fields close to the melt pool. The differences in the melt pool heat balance when using He instead of Ar turned out to be marginal. In future works, the influence of increased gas flow velocities on the heat balance and dynamics of the melt pool should be studied. These studies could be extended towards more complex and larger geometries to further support the industrial applications of PBF-LB/M.

Author Contributions: Conceptualization, S.B. and F.F.; investigation, S.B. and F.F.; methodology, S.B. and F.F.; validation, S.B. and F.F.; writing—original draft preparation, S.B. and F.F.; writing—review and editing, S.A., T.A., N.A.A. and M.F.Z.; visualization, S.B. and F.F.; supervision, S.A. and M.F.Z.; project administration, S.A. and T.A.; funding acquisition, T.A., N.A.A. and M.F.Z. All authors have read and agreed to the published version of the manuscript.

Funding: This work was supported by the project "GasAlloy-X" funded by the program "Neue Werkstoffe" from the Bavarian Ministry of Economic Affairs, Regional Development and Energy (grant number NW-1901-0013). We would like to thank the Bavarian government for that.

Data Availability Statement: The original contributions presented in the study are included in the article, further inquiries can be directed to the corresponding author.

Acknowledgments: The authors would like to thank the TUM-Oerlikon Advanced Manufacturing Institute (AMI) for supporting this project.

Conflicts of Interest: Author Thomas Ammann was employed by the company Linde GmbH. The remaining authors declare that the research was conducted in the absence of any commercial or financial relationships that could be construed as a potential conflict of interest.

Appendix A. Post-Processing in SPH

Appendix A.1. Evaluation of the Heat Flow Rate

The heat flow rate $\dot{Q}$ (i.e., the surface integral of the heat flux over the surface A) is being approximated using

$$\dot{Q} = -\oint_A (k\nabla T)\cdot \mathbf{n}\mathrm{d}A = -\sum_{\alpha\neq\beta}\left(\sum_i^N \langle k\nabla T\rangle_i \cdot \nabla C_i^{\alpha\beta} V_i\right). \tag{A1}$$

A non-symmetric smoothing operator for the heat flux gradient is used [23] according to

$$\langle k\nabla T\rangle_i = \sum_{j\in\mathbf{N}(\mathbf{r}_i)} \frac{2k_i k_j}{k_i + k_j}(T_j - T_i)\nabla_i W_{ij} V_j. \tag{A2}$$

Here, $\nabla_i W_{ij}$ denotes the gradient of the kernel function between the particle i and j and $\mathbf{N}(\mathbf{r}_i)$ denotes the set of neighboring particles of the particle i.

Appendix A.2. Evaluation of the Average Surface Temperature

The average surface temperature $\overline{T}_{\alpha\beta}$ of the α-β phase interface $A_{\alpha\beta}$ is given by

$$\overline{T}_{\alpha\beta} = \frac{\oint_{A_{\alpha\beta}} T\,\mathrm{d}A}{\oint_{A_{\alpha\beta}} \mathrm{d}A} = \frac{\sum_{\alpha\neq\beta}\left(\sum_i^N T_i \|\nabla C_i^{\alpha\beta}\| V_i\right)}{\sum_{\alpha\neq\beta}\left(\sum_i^N \|\nabla C_i^{\alpha\beta}\| V_i\right)}, \tag{A3}$$

where $\nabla C_i^{\alpha\beta}$ denotes the gradient of the color function between the α-β phase interface [49], T_i and V_i the temperature and volume of the particle i, respectively, and N the total number of particles.

Appendix B. Macroscopic Material Properties

The material properties for the Al alloy are given in Tables A1 and A2. The properties for Ar and He are given in Table A3.

Table A1. Material properties for the studied 2000 series Al alloy [41,50–53].

Material Property	Value	Unit
Mass density ρ [50]	2785.0	$\mathrm{kg\,m^{-3}}$
Solidification temperature T_s [50]	811.0	K
Liquification temperature T_l [50]	905.0	K
Boiling temperature [1] T_b [51]	2792.0	K
Surface tension coefficient [1,3] σ [50]	$0.86 - 1.8\times10^{-4}(T - 933.0)$	$\mathrm{N\,m^{-1}}$
Dynamic viscosity [3] μ [52]	$4.473\times10^{-4}\exp(965.6/T)$	$\mathrm{N\,m^{-1}}$
Thermal conductivity k [50]	Table A2	$\mathrm{W\,m^{-1}\,K^{-1}}$
Specific heat capacity C_p [50]	Table A2	$\mathrm{J\,kg^{-1}\,K^{-1}}$
Latent heat of fusion L_f [50]	297×10^3	$\mathrm{J\,kg^{-1}}$
Latent heat of evaporation [2] L_v [51]	10.025×10^3	$\mathrm{J\,kg^{-1}}$
Molar Mass [2] M [53]	29.02×10^{-3}	$\mathrm{kg\,mol^{-1}}$
Electrical resistivity [3,4] ϵ [41]	$-1.0\times10^{-8} + 1.25\times10^{-6}T + 1.93\times10^{-6}\max(0, T - T_\mathrm{s}) - 1.73\times10^{-6}\max(0, T - T_\mathrm{l})$	$\Omega\,\mathrm{m}$

[1] Value taken for pure aluminum. [2] Value was estimated on the basis of the weighted and averaged data of the chemical elements. [3] The value of T has to be inserted in the unit K based on absolute zero. [4] Reprinted with permission from [41]. Copyright 1997, Laser Institute of America.

Table A2. Temperature-dependent material properties for the studied 2000 series Al alloy following Mills [50]; k: thermal conductivity, C_p: specific heat capacity, H: enthalpy.

	Temperature T								Unit
	298	**373**	**473**	**573**	**673**	**773**	**811**	**905**	**K**
k	175	185	193	193	190	188	188	85	$W\,m^{-1}\,K^{-1}$
C_p	850	900	950	970	1000	1080	1100	1140	$J\,kg^{-1}\,K^{-1}$
H	253,300	318,925	411,425	507,425	605,925	709,925	751,345	1,048,345	$J\,kg^{-1}$

Table A3. Material properties for argon and helium [54,55].

Material Property	Argon	Helium	Units
Mass density ρ	1.6116	0.1615	$kg\,m^{-3}$
Dynamic viscosity [1] μ [54]	$4.059 \times 10^{-7} T^{0.71}$	$3.674 \times 10^{-7} T^{0.70}$	$N\,m^{-1}$
Thermal conductivity [1] k [55]	$4.9 \times 10^{-3} + 4.8 \times 10^{-5} T - 1.0 \times 10^{-8} T^2$	$4.5 \times 10^{-2} + 3.641 \times 10^{-4} T - 4.58 \times 10^{-8} T^2$	$W\,m^{-1}\,K^{-1}$
Specific heat capacity C_p	520	5193	$J\,kg^{-1}\,K^{-1}$

[1] The value of T has to be inserted in the unit K based on absolute zero.

Appendix C. AconityMINI PBF-LB/M Machine

A picture of the AconityMINI PBF-LB/M machine is given in Figure A1.

Figure A1. Picture of the AconityMINI PBF-LB/M machine.

References

1. Qin, Y.; Liu, J.; Chen, Y.; Wen, P.; Zheng, Y.; Tian, Y.; Voshage, M.; Schleifenbaum, J.H. Influence of Laser Energy Input and Shielding Gas Flow on Evaporation Fume during Laser Powder Bed Fusion of Zn Metal. *Materials* **2021**, *14*, 2677. [CrossRef] [PubMed]
2. Ladewig, A.; Schlick, G.; Fisser, M.; Schulze, V.; Glatzel, U. Influence of the shielding gas flow on the removal of process by-products in the selective laser melting process. *Addit. Manuf.* **2016**, *10*, 1–9. [CrossRef]
3. Yang, Y.; Chen, Z.; Liu, Z.; Wang, H.; Zhang, Y.; Wang, D. Influence of shielding gas flow consistency on parts quality consistency during large-scale laser powder bed fusion. *Opt. Laser Technol.* **2023**, *158*, 108899. [CrossRef]

4. Baehr, S.; Klecker, T.; Pielmeier, S.; Ammann, T.; Zaeh, M.F. Experimental and analytical investigations of the removal of spatters by various process gases during the powder bed fusion of metals using a laser beam. *Prog. Addit. Manuf.* **2023**, *9*, 905–917. [CrossRef]
5. Pauzon, C.; Hoppe, B.; Pichler, T.; Dubiez-Le Goff, S.; Forêt, P.; Nguyen, T.; Hryha, E. Reduction of incandescent spatter with helium addition to the process gas during laser powder bed fusion of Ti-6Al-4V. *CIRP J. Manuf. Sci. Technol.* **2021**, *35*, 371–378. [CrossRef]
6. Weaver, J.S.; Schlenoff, A.; Deisenroth, D.C.; Moylan, S.P. *Inert Gas Flow Speed Measurements in Laser Powder Bed Fusion Additive Manufacturing*; NIST Advanced Manufacturing Series 100-43; National Institute of Standards and Technology: Gaithersburg, MD, USA, 2021; pp. 1–18. [CrossRef]
7. DebRoy, T.; Wei, H.L.; Zuback, J.S.; Mukherjee, T.; Elmer, J.W.; Milewski, J.O.; Beese, A.M.; Wilson-Heid, A.; De, A.; Zhang, W. Additive manufacturing of metallic components—Process, structure and properties. *Prog. Mater. Sci.* **2018**, *92*, 112–224. [CrossRef]
8. Li, Y.; Gu, D. Parametric analysis of thermal behavior during selective laser melting additive manufacturing of aluminum alloy powder. *Mater. Des.* **2014**, *63*, 856–867. [CrossRef]
9. Masoomi, M.; Pegues, J.W.; Thompson, S.M.; Shamsaei, N. A numerical and experimental investigation of convective heat transfer during laser-powder bed fusion. *Addit. Manuf.* **2018**, *22*, 729–745. [CrossRef]
10. Gingold, R.A.; Monaghan, J.J. Smoothed particle hydrodynamics: Theory and application to non-spherical stars. *Mon. Not. R. Astron. Soc.* **1977**, *181*, 375–389. [CrossRef]
11. Marrone, S.; Antuono, M.; Colagrossi, A.; Colicchio, G.; Le Touzé, D.; Graziani, G. δ-SPH model for simulating violent impact flows. *Comput. Methods Appl. Mech. Eng.* **2011**, *200*, 1526–1542. [CrossRef]
12. Vila, J.P. On particle weighted methods and smooth particle hydrodynamics. *Math. Model. Methods Appl. Sci.* **1999**, *9*, 161–209. [CrossRef]
13. Monaghan, J.J. SPH and Riemann solvers. *J. Comput. Phys.* **1997**, *136*, 298–307. [CrossRef]
14. Russell, M.; Souto-Iglesias, A.; Zohdi, T. Numerical simulation of Laser Fusion Additive Manufacturing processes using the SPH method. *Comput. Methods Appl. Mech. Eng.* **2018**, *341*, 163–187. [CrossRef]
15. Afrasiabi, M.; Keller, D.; Lüthi, C.; Bambach, M.; Wegener, K. Effect of process parameters on melt pool geometry in laser powder bed fusion of metals: A numerical investigation. *Procedia CIRP* **2022**, *113*, 378–384. [CrossRef]
16. Weirather, J.; Rozov, V.; Wille, M.; Schuler, P.; Seidel, C.; Adams, N.A.; Zaeh, M.F. A smoothed particle hydrodynamics model for laser beam melting of Ni-based alloy 718. *Comput. Math. Appl.* **2019**, *78*, 2377–2394. [CrossRef]
17. Morris, J.P.; Fox, P.J.; Zhu, Y. Modeling Low Reynolds Number Incompressible Flows Using SPH. *J. Comput. Phys.* **1997**, *136*, 214–226. [CrossRef]
18. Adami, S.; Hu, X.; Adams, N.A. A transport-velocity formulation for smoothed particle hydrodynamics. *J. Comput. Phys.* **2013**, *241*, 292–307. [CrossRef]
19. Monaghan, J.J. SPH without a tensile instability. *J. Comput. Phys.* **2000**, *159*, 290–311. [CrossRef]
20. Brackbill, J.U.; Kothe, D.B.; Zemach, C. A continuum method for modeling surface tension. *J. Comput. Phys.* **1992**, *100*, 335–354. [CrossRef]
21. Zöller, C.; Adams, N.; Adami, S. A partitioned continuous surface stress model for multiphase smoothed particle hydrodynamics. *J. Comput. Phys.* **2023**, *472*, 111716. [CrossRef]
22. Cleary, P.W. Modelling confined multi-material heat and mass flows using SPH. *Appl. Math. Model.* **1998**, *22*, 981–993. [CrossRef]
23. Cleary, P.W.; Monaghan, J.J. Conduction modelling using smoothed particle hydrodynamics. *J. Comput. Phys.* **1999**, *148*, 227–264. [CrossRef]
24. Anisimov, S.I.; Khokhlov, V.A. *Instabilities in Laser-Matter Interaction*; CRC Press: Boca Raton, FL, USA, 1995.
25. Khairallah, S.A.; Anderson, A.T.; Rubenchik, A.; King, W.E. Laser powder-bed fusion additive manufacturing: Physics of complex melt flow and formation mechanisms of pores, spatter, and denudation zones. *Acta Mater.* **2016**, *108*, 36–45. [CrossRef]
26. Semak, V.V.; Bragg, W.D.; Damkroger, B.; Kempka, S. Transient model for the keyhole during laser welding. *J. Phys. D Appl. Phys.* **1999**, *32*, L61. [CrossRef]
27. Semak, V.; Matsunawa, A. The role of recoil pressure in energy balance during laser materials processing. *J. Phys. D Appl. Phys.* **1997**, *30*, 2541. [CrossRef]
28. Semak, V.; Hopkins, J.; McCay, M.; McCay, T. A concept for a hydrodynamic model of keyhole formation and support during laser welding. *Int. Congr. Appl. Lasers Electro-Opt.* **1994**, *1*, 641–650. [CrossRef]
29. Zohdi, T. Simulation of coupled microscale multiphysical-fields in particulate-doped dielectrics with staggered adaptive FDTD. *Comput. Methods Appl. Mech. Eng.* **2010**, *199*, 3250–3269. [CrossRef]
30. Khairallah, S.A.; Chin, E.B.; Juhasz, M.J.; Dayton, A.L.; Capps, A.; Tsuji, P.H.; Bertsch, K.M.; Perron, A.; Mccall, S.K.; Mckeown, J.T. High fidelity model of directed energy deposition: Laser-powder-melt pool interaction and effect of laser beam profile on solidification microstructure. *Addit. Manuf.* **2023**, *73*, 103684. [CrossRef]
31. Khairallah, S.A.; Sun, T.; Simonds, B.J. Onset of periodic oscillations as a precursor of a transition to pore-generating turbulence in laser melting. *Addit. Manuf. Lett.* **2021**, *1*, 100002. [CrossRef]
32. Zenz, C.; Buttazzoni, M.; Florian, T.; Armijos, K.E.C.; Vázquez, R.G.; Liedl, G.; Otto, A. A compressible multiphase Mass-of-Fluid model for the simulation of laser-based manufacturing processes. *Comput. Fluids* **2024**, *268*, 106109. [CrossRef]

33. Shah, D.; Volkov, A.N. Combined smoothed particle hydrodynamics-ray tracing method for simulations of keyhole formation in laser melting of bulk and powder metal targets. In *Proceedings of the ASME International Mechanical Engineering Congress and Exposition*; American Society of Mechanical Engineers: Salt Lake City, UT, USA, 2019; Volume 59377, pp. 1–8. [CrossRef]
34. Shah, D.; Volkov, A.N. Simulations of deep drilling of metals by continuous wave lasers using combined smoothed particle hydrodynamics and ray-tracing methods. *Appl. Phys. A* **2020**, *126*, 82. [CrossRef]
35. Khairallah, S.; Anderson, A.; Rubenchik, A.; Florando, J.; Wu, S.; Lowdermilk, H. Simulation of the main physical processes in remote laser penetration with large laser spot size. *AIP Adv.* **2015**, *5*, 047120. [CrossRef]
36. Jadhav, S.D.; Goossens, L.R.; Kinds, Y.; Van Hooreweder, B.; Vanmeensel, K. Laser-based powder bed fusion additive manufacturing of pure copper. *Addit. Manuf.* **2021**, *42*, 101990. [CrossRef]
37. Adami, S.; Hu, X.Y.; Adams, N.A. A generalized wall boundary condition for smoothed particle hydrodynamics. *J. Comput. Phys.* **2012**, *231*, 7057–7075. [CrossRef]
38. Lastiwka, M.; Basa, M.; Quinlan, N.J. Permeable and non-reflecting boundary conditions in SPH. *Int. J. Numer. Methods Fluids* **2009**, *61*, 709–724. [CrossRef]
39. Price, D.J. Smoothed particle hydrodynamics and magnetohydrodynamics. *J. Comput. Phys.* **2012**, *231*, 759–794. [CrossRef]
40. Zhang, Z.; Zhang, T.; Sun, C.; Karna, S.; Yuan, L. Understanding Melt Pool Behavior of 316L Stainless Steel in Laser Powder Bed Fusion Additive Manufacturing. *Micromachines* **2024**, *15*, 170. [CrossRef]
41. Xie, J.; Kar, A.; Rothenflue, J.A.; Latham, W.P. Temperature-dependent absorptivity and cutting capability of CO2, Nd: YAG and chemical oxygen–iodine lasers. *J. Laser Appl.* **1997**, *9*, 77–85. [CrossRef]
42. Baehr, S.; Melzig, L.; Bauer, D.; Ammann, T.; Zaeh, M.F. Investigations of process by-products by means of Schlieren imaging during the powder bed fusion of metals using a laser beam. *J. Laser Appl.* **2022**, *34*, 042045. [CrossRef]
43. Wang, J.; Zhu, R.; Liu, Y.; Zhang, L. Understanding melt pool characteristics in laser powder bed fusion: An overview of single- and multi-track melt pools for process optimization. *Adv. Powder Mater.* **2023**, *2*, 100137. [CrossRef]
44. Forien, J.B.; Calta, N.P.; Depond, P.J.; Guss, G.M.; Roehling, T.T.; Matthews, M.J. Detecting keyhole pore defects and monitoring process signatures during laser powder bed fusion: A correlation between in situ pyrometry and ex situ X-ray radiography. *Addit. Manuf.* **2020**, *35*, 101336. [CrossRef]
45. Chaudry, M.A.; Mohr, G.; Hilgenberg, K. Experimental and numerical comparison of heat accumulation during laser powder bed fusion of 316L stainless steel. *Prog. Addit. Manuf.* **2022**, *7*, 1071–1083. [CrossRef]
46. Kempen, K.; Thijs, L.; van Humbeeck, J.; Kruth, J.P. Processing AlSi10Mg by selective laser melting: Parameter optimisation and material characterisation. *Mater. Sci. Technol.* **2015**, *31*, 917–923. [CrossRef]
47. Hooper, P.A. Melt pool temperature and cooling rates in laser powder bed fusion. *Addit. Manuf.* **2018**, *22*, 548–559. [CrossRef]
48. Deckers, T.; Fardan, A.; Kersting, L.; Kreutzer, A.; Foret, P.; Dubiez-Le Goff, S.; Witt, G.; Kleszczynski, S.; Klement, U.; Hryha, E. Impact of processing gas composition on process stability and properties of PBF-LB/M processed alloy 718. *J. Manuf. Process.* **2024**, *120*, 712–718. [CrossRef]
49. Hu, X.Y.; Adams, N.A. A multi-phase SPH method for macroscopic and mesoscopic flows. *J. Comput. Phys.* **2006**, *213*, 844–861. [CrossRef]
50. Mills, K.C. *Recommended Values of Thermophysical Properties for Selected Commercial Alloys*; Woodhead Publishing: Cambridge, UK, 2002.
51. Zhang, Y.; Evans, J.R.G.; Yang, S. Corrected Values for Boiling Points and Enthalpies of Vaporization of Elements in Handbooks. *J. Chem. Eng. Data* **2011**, *56*, 328–337. [CrossRef]
52. Valencia, J.J.; Quested, P.N. Thermophysical properties. In *Modeling for Casting and Solidification Processing*; ASM International: Almere, The Netherlands, 2013.
53. De Laeter, J.R.; Böhlke, J.K.; De Bievre, P.; Hidaka, H.; Peiser, H.; Rosman, K.; Taylor, P. Atomic weights of the elements. Review 2000 (IUPAC Technical Report). *Pure Appl. Chem.* **2003**, *75*, 683–800. [CrossRef]
54. Petersen, H. *The Properties of Helium: Density, Specific Heats, Viscosity, and Thermal Conductivity at Pressures from 1 to 100 Bar and from Room Temperature to About 1800 K*; Jul. Gjellerup Copenhagen; Risø National Laboratory: Roskilde, Denmark, 1970.
55. Purohit, A.; Moszynaki, J. *Thermal Conductivity of the Helium-Argon System*; Technical Report; Argonne National Lab.: Argonne, IL, USA, 1979.